Charging and discharging characteristics of absorption thermal energy storage using ionic-liquid-based working fluids

Wei Wu [a, *], Yu Bai [b], Hongyu Huang [b], Zhixiong Ding [a], Lisheng Deng [b]

[a] *School of Energy and Environment, City University of Hong Kong, Hong Kong, China*
[b] *Urban-rural Mine Integrated Technology Research Team, Guangzhou Institute of Energy Conversion, Chinese Academy of Sciences, Guangzhou, China*

ABSTRACT

The absorption thermal energy storage (ATES) systems using H_2O/ionic liquid (IL) mixtures as novel working fluids are explored to avoid the crystallization problem. The property model and cycle model are established and validated against experimental data. The dynamic charging/discharging characteristics and overall cycle performance are compared for four ILs ([DMIM][DMP], [EMIM][Ac], [EMIM][DEP], and [EMIM][EtSO$_4$]). Under a typical condition, [DMIM][DMP] yields the highest coefficient of performance (COP) of 0.722 while [EMIM][DEP] yields the lowest COP of 0.603; [DMIM][DMP] shows the highest energy storage density (ESD) of 94.1 kW h/m^3 while [EMIM][DEP] shows the lowest ESD of 77.5 kW h/m^3; [EMIM][Ac] needs the longest charging time of 107.5 min, while [EMIM][EtSO$_4$] needs the longest discharging time of 207.0 min. Being the best-performing IL in terms of high COP and ESD, [DMIM][DMP] has been further investigated, with charging temperatures of 85−100 °C, cooling water temperatures of 25−35 °C and discharging temperatures of 9−15 °C. The highest COP is 0.761 and the highest ESD is 149.5 kW h/m^3 in the investigated operating conditions. In summary, it is feasible to use H_2O/ILs as crystallization-free working fluids of the ATES systems. This study aims to provide theoretical references and suggestions for the selection of novel working fluids for the ATES systems.

© 2019 Elsevier Ltd. All rights reserved.

1. Introduction

The building energy consumption typically accounts for 20−40% of the territory total energy use, making building energy efficiency a significant measure for mitigating the global warming issues [1]. Heating, ventilating and air-conditioning (HVAC) is one of the largest energy consumers in buildings, leading to increasing interests in utilization of renewable energy and waste heat for HVAC energy efficiency [2]. Due to the mismatch of timing and intensity between the renewable/waste energy sources and the time-variable building cooling/heating loads, thermal energy storage (TES) technologies are necessary to balance the energy supply and energy demand [3,4].

There have been a variety of TES technologies, including sensible TES, latent TES, and thermochemical TES [5]. The performance characteristics of TES systems are evaluated by different indexes, including energy storage density (ESD), coefficient of performance (COP), applicable charging temperature, and charging/discharging

rate. The sensible TES systems, e.g., heat storage in water, soil, and aquifer, suffer from low ESDs due to the small capacities during temperature changes [6]. For the latent TES systems, ice cold storage shows low COPs due to low chilled water temperatures, while PCM (phase change material) heat storage shows low charging/discharging rates due to low thermal conductivities [7,8]. The thermochemical TES includes chemical reaction, solid adsorption, and liquid absorption [9,10]. The chemical reaction TES systems have high ESDs but require high charging temperature (e.g., above 200 °C), while the solid adsorption TES systems require low charging temperatures but suffer from low COPs [11]. The liquid absorption thermal energy storage (ATES) attracts increasing interests owing to better comprehensive performance, i.e., relatively high COPs, high ESDs and low charging temperatures [12]. In addition, the ATES has a wider flexibility in applications because the energy can be discharged in various forms (cooling, heating and dehumidification) depending on the requirements.

Working fluids play an important role in determining the performance of the ATES systems. The most commonly studied working fluids are H_2O-based [13,14] and NH_3-based [15] mixtures. The H_2O-based mixtures (e.g., H_2O/LiBr and H_2O/LiCl) have high

Nomenclature

B	second virial coefficient, cm^3/mol
C_p	specific heat capacity, $kJ/(kg \cdot K)$
C_{pm}	molar heat capacity, $J/(mol \cdot K)$
h	mass-based enthalpy, kJ/kg
H	mole-based enthalpy, J/mol
$\dot{m}$	mass flow rate, kg/s
M	mass, kg
p	pressure, kPa
q	heat duty, kW
Q	cumulative thermal energy, kWh
R	universal gas constant, $J/(mol \cdot K)$
t	temperature, $°C$
T	temperature, K
UA	product of heat transfer coefficient and heat transfer area, $kW/°C$
V	volume, m^3, cm^3/mol
x	liquid mass fraction
X	liquid mole fraction
Y	vapor mole fraction
α	adjustable parameters
τ	time, s; adjustable parameters
γ	activity coefficient
ρ	density, kg/m^3
Φ	correction factor

Abbreviations

ATES	absorption thermal energy storage
COP	coefficient of performance
ESD	energy storage density
HVAC	heating, ventilating and air-conditioning
IL	ionic liquid
NRTL	non-random two liquid
PCM	phase change material
TES	thermal energy storage
VLE	vapor-liquid equilibrium

Subscripts and Superscripts

a	absorber
c	condenser
e	evaporator
g	generator
i	inlet, species index
lr	liquid refrigerant
L	liquid
mix	mixing
o	outlet
r	refrigerant
s	saturation, solution
vr	vapor refrigerant

COPs and ESDs but cannot be used for sub-zero evaporation temperatures (including cold discharge and heat discharge) due to the high freezing point of refrigerant H_2O [16]. The NH_3-based mixtures (e.g., NH_3/H_2O) are suitable options for sub-zero evaporation temperatures, but the performance is relatively worse, and the toxicity is a concern [17].

There have been many studies on ATES using various working fluids. Weber and Dorer [18] tested a $H_2O/NaOH$ ATES, requiring a solar heat input at $150\,°C$, for long-term heat storage. Compared to conventional water storage, the ESD was increased by a factor of 6 for low-temperature space heating ($40\,°C$) and by a factor of 3 for water heating ($65-70\,°C$). Xu et al. [19] analyzed a solar-powered $H_2O/LiBr$ absorption refrigeration system with ATES. The results showed a COP around 0.75 and an ESD about $368.5\,MJ/m^3$. El-Shaarawi et al. [20] explored the impact of unsteady solar intensity and ambient conditions on the performance of an NH_3/H_2O absorption chiller with ATES. The COP was better in winter than in summer (0.57 as compared to 0.39) but the required solar collector was larger in winter than in summer. They also analyzed the system using $H_2O/LiBr$ and drawn similar conclusions [21]. Zhang et al. [22] measured the charging and discharging processes of $H_2O/LiBr$ ATES systems producing $7\,°C$ chilled water (space cooling), $65\,°C$ hot water (water heating) and $43\,°C$ hot water (space heating). The COPs were 0.51, 0.97 and 1.03, while the ESDs were 42, 88 and $110\,kW\,h/m^3$, respectively. Fumey et al. [23] investigated a $H_2O/NaOH$ ATES for seasonal heat storage, with the heat and mass exchangers developed on a tube bundle falling film basis. The testing of heat discharging process showed absorption much slower than expected, due to limited tube wetting and absorption speed. Zhao et al. [24] introduced the electrical circuit analogy to analyze and optimize the $H_2O/LiBr$ ATES systems. The optimized results offered 13% and 25% higher power (as compared to existing experimental results) in the charging and discharging processes.

Different working fluids have also been compared for the ATES systems. Mugnier and Goetz [25] compared the ESDs of different working fluids, including $H_2O/CH_3NH_2/LiBr$, $CH_3NH_2/LiSCN$, $CH_3OH/LiBr$, $H_2O/CH_3OH/LiBr$, H_2O/H_2SO_4, $H_2O/LiBr$, $H_2O/NaOH$, NH_3/H_2O, $NH_3/H_2O/LiBr$, $NH_3/H_2O/LiNO_3$, $NH_3/LiNO_3$ and $NH_3/NaSCN$. With a heat source temperature of $180\,°C$, $H_2O/NaOH$ yielded the highest mass-based ESD of $260\,W\,h/kg$ for normal-temperature cold storage (an evaporation temperature of $5\,°C$), while NH_3/H_2O showed the highest mass-based ESD of $95\,W\,h/kg$ for low-temperature cold storage (an evaporation temperature of $-20\,°C$). Liu et al. [26] compared the ESDs, COPs, charging temperatures, economics and corrosion of an ATES for long-term solar heat storage using different working fluids, including $H_2O/CaCl_2$, $H_2O/Glycerin$, H_2O/KOH, $H_2O/LiBr$, $H_2O/LiCl$, $H_2O/NaOH$, and H_2O/NH_3. They found that $H_2O/LiCl$ had high ESD and COP but was expensive; H_2O/KOH had high ESD and low cost but was too corrosive; $H_2O/CaCl_2$ was inexpensive but showed low ESD; $H_2O/LiBr$ was the best choice considering different factors comprehensively.

The literature review indicated that H_2O-based working fluids are more widely used for ATES systems owing to their high COPs and ESDs. However, most $H_2O/salt$ mixtures have a risk of crystallization when the salt concentration is too high, or the solution temperature is too low. Some researchers studied the feasibility of three-phase ATES (with crystallization) for the working fluids like $H_2O/LiBr$ [27,28], $H_2O/LiCl$ [29] and $H_2O/CaCl_2$ [30]. Although with improved ESDs, the accumulated crystallization might be difficult to dissolve, which affects the composition of the working fluid and the sustainability of the ATES system. This concern exists in both short-term and long-term storage applications and can be more serious for long-term storage.

To address this problem, novel working fluids based on ionic liquids (ILs) are explored for the ATES systems. The ILs have attracted increasing interests due to their negligible vapor pressure, good stability and high solubility with various refrigerants [31]. The investigated IL-based mixtures include H_2O/IL, NH_3/IL, alcohol/IL, HFC/IL, HFO/IL and CO_2/IL [31-35], but all used for absorption chillers or heat pumps. There is little research on IL-based working

fluids for ATES systems. This work focuses on the ATES using H_2O/ILs as novel working fluids. The ATES can be charged to more concentrated solutions without crystallization, aiming to enhance the ESD and reliability. The dynamic behaviors of charging and discharging processes will be characterized to explore the ATES performance under different operating conditions. In addition, different H_2O/ILs will be investigated to identify the best-performing alternative.

2. Methodology

2.1. ATES cycle model

The schematic diagram of the ATES system is shown in Fig. 1. It mainly consists of a solution tank and a refrigerant tank, with a heat exchanger inside each tank. In the charging process, the solution tank acts as a generator and is heated by the external heat source to produce vapor H_2O; the refrigerant tank acts as a condenser and is cooled by the external cooling water to liquified the vapor H_2O. With vapor H_2O generated from the solution tank, the H_2O/IL solution gets more and more concentrated and the thermal energy is stored in the solution tank. In the discharging process, taking cold discharging for instance, the refrigerant tank becomes an evaporator and produces cooling effect while the liquid H_2O evaporates; the solution tank becomes an absorber and is cooled by the external cooling water to maintain the absorption between solution and vapor H_2O.

To establish the model of the ATES cycle, some reasonable assumptions are made for simplification: (1) the heat capacities of the walls of heat exchangers are neglected; (2) the pressure drops and heat losses of the tanks and heat exchangers are ignored; (3) the solution temperatures in the solution tank are uniform, and the refrigerant temperatures in the refrigerant tank are uniform; and (4) the overall heat transfer coefficients of heat exchangers are regarded as constants; (5) the simulation case is based on a short-term storage, so that the sensible heat loss during the storage period is ignored. With these assumptions, the dynamic model of the charging and discharging processes are built based on the mass conservation, energy conservation and heat transfer equations. The flow chart of the calculation algorithm is shown in Fig. A1 in the Appendix.

2.1.1. Charging process

The mass conservations the solution, the absorbent and the refrigerant are governed by:
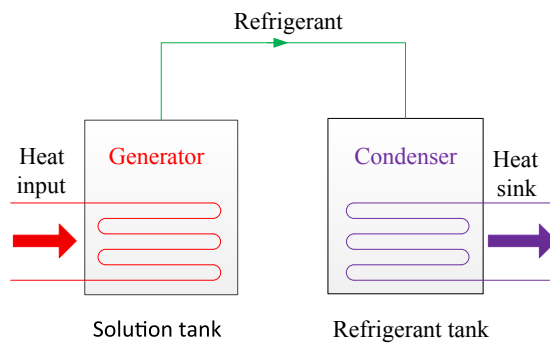
$$\frac{dM_s(\tau)}{d\tau} = -\dot{m}_{vr}(\tau) \tag{1}$$

$$\frac{d[M_s(\tau)(1 - x_s(\tau))]}{d\tau} = 0 \tag{2}$$

$$\frac{dM_{lr}(\tau)}{d\tau} = \dot{m}_{vr}(\tau) \tag{3}$$

where M_s and M_{lr} are respectively the mass of solution in the solution tank and liquid refrigerant in the refrigerant tank; $\dot{m}_{vr}$ is the mass flow rate of the generated vapor refrigerant; τ is time; x_s is the refrigerant fraction in the solution tank.

The energy conservations and heat transfer processes in the generator (solution tank) are expressed by:

$$\frac{d[M_s(\tau)h_s(\tau)]}{d\tau} = q_g(\tau) - h_{vr}(\tau)\dot{m}_{vr}(\tau) \tag{4}$$

$$q_g(\tau) = c_p \dot{m}_g(\tau)[t_{gi}(\tau) - t_{go}(\tau)] \tag{5}$$

$$q_g(\tau) = UA_g \Delta t_g(\tau) = \frac{UA_g[t_{gi}(\tau) - t_{go}(\tau)]}{\ln\left[\frac{t_{gi}(\tau) - t_g(\tau)}{t_{go}(\tau) - t_g(\tau)}\right]} \tag{6}$$

where h_s and h_{vr} are respectively the specific enthalpies of solution and vapor refrigerant; $\dot{m}_g$ is the mass flow rate of the external heat source of the generator; q_g is the heat duty of the generator; c_p is the specific heat of the external mediums; UA_g is the product of heat transfer coefficient and heat transfer area of the generator; Δt_g is the logarithm-mean temperature difference of the generator; t_g, t_{gi} and t_{go} are the generation temperature, generator inlet temperature and generator outlet temperature.
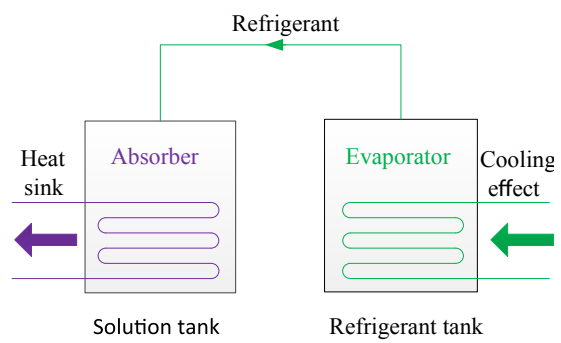
The energy conservations and heat transfer processes in the condenser (refrigerant tank) are expressed by:

$$\frac{d[M_{lr}(\tau)h_{lr}(\tau)]}{d\tau} = -q_c(\tau) + h_{vr}(\tau)\dot{m}_{vr}(\tau) \tag{7}$$

$$q_c(\tau) = c_p \dot{m}_c(\tau)[t_{co}(\tau) - t_{ci}(\tau)] \tag{8}$$

$$q_c(\tau) = UA_c \Delta t_c(\tau) = \frac{UA_c[t_{co}(\tau) - t_{ci}(\tau)]}{\ln\left[\frac{t_c(\tau) - t_{ci}(\tau)}{t_c(\tau) - t_{co}(\tau)}\right]} \tag{9}$$

where h_{lr} is the specific enthalpy of liquid refrigerant; $\dot{m}_c$ is the

Fig. 1. Schematic diagram of the ATES system.

mass flow rate of the external cooling water of the condenser; q_c is the heat duty of the condenser; UA_c is the product of heat transfer coefficient and heat transfer area of the condenser; Δt_c is the logarithm-mean temperature difference of the condenser; t_c, t_{ci} and t_{co} are the condensation temperature, condenser inlet temperature and condenser outlet temperature.

The total charged thermal energy and rejected thermal energy are the integrations of $q_g(\tau)$ and $q_c(\tau)$ over the charging time:

$$Q_g = \int q_g(\tau), \quad Q_c = \int q_c(\tau) \tag{10}$$

2.1.2. Discharging process

The mass conservations of the solution, the absorbent and the refrigerant are governed by:

$$\frac{dM_s(\tau)}{d\tau} = \dot{m}_{vr}(\tau) \tag{11}$$

$$\frac{d[M_s(\tau)(1 - x_s(\tau))]}{d\tau} = 0 \tag{12}$$

$$\frac{dM_{lr}(\tau)}{d\tau} = -\dot{m}_{vr}(\tau) \tag{13}$$

The energy conservations and heat transfer processes in the absorber (solution tank) are expressed by:

$$\frac{d[M_s(\tau)h_s(\tau)]}{d\tau} = -q_a(\tau) + h_{vr}(\tau)\dot{m}_{vr}(\tau) \tag{14}$$

$$q_a(\tau) = c_p \dot{m}_a(\tau)[t_{ao}(\tau) - t_{ai}(\tau)] \tag{15}$$

$$q_a(\tau) = UA_a \Delta t_a(\tau) = \frac{UA_a[t_{ao}(\tau) - t_{ai}(\tau)]}{\ln\left[\frac{t_a(\tau) - t_{ai}(\tau)}{t_a(\tau) - t_{ao}(\tau)}\right]} \tag{16}$$

where $\dot{m}_a$ is the mass flow rate of the external cooling water of the absorber; q_a is the heat duty of the absorber; UA_a is the product of heat transfer coefficient and heat transfer area of the absorber; Δt_a is the logarithm-mean temperature difference of the absorber; t_a, t_{ai} and t_{ao} are the absorption temperature, absorber inlet temperature and absorber outlet temperature.

The energy conservations and heat transfer processes in the evaporator (refrigerant tank) are expressed by:

$$\frac{d[M_{lr}(\tau)h_{lr}(\tau)]}{d\tau} = q_e(\tau) - h_{vr}(\tau)\dot{m}_{vr}(\tau) \tag{17}$$

$$q_e(\tau) = c_p \dot{m}_e(\tau)[t_{ei}(\tau) - t_{eo}(\tau)] \tag{18}$$

$$q_e(\tau) = UA_e \Delta t_e(\tau) = \frac{UA_e[t_{ei}(\tau) - t_{eo}(\tau)]}{\left[\frac{t_{ei}(\tau) - t_e(\tau)}{t_{eo}(\tau) - t_e(\tau)}\right]} \tag{19}$$

where $\dot{m}_e$ is the mass flow rate of the external chilled water of the evaporator; q_e is the heat duty of the evaporator; UA_e is the product of heat transfer coefficient and heat transfer area of the evaporator; Δt_e is the logarithm-mean temperature difference of the evaporator; t_e, t_{ei} and t_{eo} are the evaporation temperature, evaporator inlet temperature and evaporator outlet temperature.

The total discharged cold energy and rejected thermal energy are the integrations of $q_e(\tau)$ and $q_a(\tau)$ over the discharging time:

$$Q_e = \int q_e(\tau), \quad Q_a = \int q_a(\tau) \tag{20}$$

The COP of the ATES cycle is defined as the ratio of the total discharged energy over the total charged energy:

$$COP = \frac{Q_e}{Q_g} \tag{21}$$

The ESD of the ATES cycle is defined as the ratio of the total discharged energy over the total volume of the solution tank and refrigerant tank:

$$ESD = \frac{Q_e}{V_s + V_r} \tag{22}$$

where V_s and V_r are the volumes of the solution tank and refrigerant tank, which are determined by the liquid mass and density. The volumes of accessories are not considered following the convention of the studies on ATES systems [22].

2.2. H$_2$O/IL property model

Based on our previous studies on the H$_2$O/IL mixtures with adequate experiment data, four ILs with better performance are chosen for investigation in this work. The basic information of the selected ILs is listed in Table 1.

The non-random two liquid (NRTL) model is adopted to correlate the vapor-liquid equilibrium (VLE), i.e., the relationship among pressure, temperature and concentration [36,37]:

$$Y_i p \Phi_i = X_i \gamma_i p_i^S (i = 1, 2), \tag{23}$$

$$\Phi_i = exp\left[\frac{\left(B_i - V_i^L\right)\left(p - p_i^S\right)}{RT}\right] \tag{24}$$

where index 1 and 2 represent H$_2$O and IL, respectively; X_i and Y_i are the liquid and vapor molar fractions of refrigerant; Y_1 is 1 (the neglected IL fraction in the vapor phase); p is the mixture pressure; Φ_i is the correction factor; p_i^S is the saturated vapor pressure; γ_i is the activity coefficient; B_i is the second virial coefficient; V_i^L is the saturated molar liquid volume. The refrigerant properties were obtained from Refprop [38];

The activity coefficients of the H$_2$O/IL mixtures are calculated by Ref. [36]:

$$\ln\gamma_1 = X_2^2\left[\frac{\tau_{21}G_{21}^2}{(X_1 + X_2 G_{21})^2} + \frac{\tau_{12}G_{12}}{(X_2 + X_1 G_{12})^2}\right] \tag{25}$$

$$\ln\gamma_2 = X_1^2\left[\frac{\tau_{12}G_{12}^2}{(X_2 + X_1 G_{12})^2} + \frac{\tau_{21}G_{21}}{(X_1 + X_2 G_{21})^2}\right] \tag{26}$$

$$G_{12} = \exp(-\alpha\tau_{12}), G_{21} = \exp(-\alpha\tau_{21}) \tag{27}$$

$$\tau_{12} = \tau_{12}^0 + \frac{\tau_{12}^1}{T}, \tau_{21} = \tau_{21}^0 + \frac{\tau_{21}^1}{T} \tag{28}$$

where α, τ_{12}^0, τ_{12}^1, τ_{21}^0 and τ_{21}^1 are adjustable parameters regressed from experimental data [39–42]. The regressed adjustable parameters of the selected H$_2$O/IL mixtures are presented in Table 2

The enthalpies of the H$_2$O/IL mixtures are calculated by Refs. [31,43]:

Table 1
Basic information of the selected ILs.

Abbreviation	Full name	Molecular Formula	Molecular weight
[DMIM][DMP]	1,3-dimethylimidazolium dimethylphosphate	$C_7H_{15}N_2O_4P$	222.18
[EMIM][Ac]	1-ethyl-3-methylimidazolium acetate	$C_8H_{14}N_2O_2$	170.21
[EMIM][DEP]	1-ethyl-3-methylimidazolium diethylphosphate	$C_{10}H_{21}N_2O_4P$	264.26
[EMIM][EtSO$_4$]	1-ethyl-3-methylimidazolium ethylsulfate	$C_8H_{16}N_2O_4S$	236.29

Table 2
Adjustable parameters of the NRTL model for selected H_2O/IL mixtures.

H_2O/IL mixture	α	τ_{12}^0	τ_{12}^1	τ_{21}^0	τ_{21}^1
[DMIM][DMP] [39]	−0.086	−4.442	−3283.680	3.644	−645.872
[EMIM][Ac] [40]	0.233	−15.891	8395.751	−2.828	−952.830
[EMIM][DEP] [41]	0.070	21.710	−1999.990	−6.694	−1999.990
[EMIM][EtSO$_4$] [42]	1.499	3.674	−1301.384	1.347	−906.562

$$H = X_1 H_1 + X_2 H_2 + \Delta H_{\text{mix}} \qquad (29)$$

$$H_2 = \int_{T_0}^{T} C_{\text{pm, IL}} dT + H_0 \qquad (30)$$

$$\Delta H_{mix} = -RT^2 \left[X_1 \left(\frac{\partial \ln \gamma_1}{\partial T} \right)_{p,X} + X_2 \left(\frac{\partial \ln \gamma_2}{\partial T} \right)_{p,X} \right] \qquad (31)$$

where H_1 and H_2 are the molar enthalpies of liquid H_2O and IL, respectively; ΔH_{mix} is the mixing enthalpy; H_0 is the reference enthalpy at the reference temperature T_0 (273.15 K); R is the univeral gas constant (8.314472 J/(mol·K)); $C_{\text{pm, IL}}$ is the molar heat capacity of ILs regressed from experimental data:

$$C_{\text{pm, IL}} = C_0 + C_1 T \qquad (32)$$

The densities of the H_2O/IL mixtures are estimated by Ref. [44]:

$$\rho = x_1 \rho_1 + x_2 \rho_2 \qquad (33)$$

$$\rho_2 = D_0 + D_1 T \qquad (34)$$

where x_1 and x_2 are the mass fractions of H_2O and IL, respectively; ρ_1 and ρ_2 are the densities of the liquid H_2O and IL. The regressed coefficients of heat capacities (Eq. (32)) and densities (Eq. (34)) of the selected ILs are presented in Table 3.

2.3. Model validation

Both the property model and the cycle model are validated against the experimental data to guarantee the accuracy of the predicted results. For the NRTL property model, the calculated pressures and the measured pressures of two H_2O/IL mixtures ([EMIM][Ac] and [EMIM][EtSO$_4$]) under a range of concentrations and temperatures are compared in Fig. 2. The calculated pressures

Table 3
Coefficients of heat capacities and densities of selected ILs.

IL	C_0	C_1	D_0	D_1
[DMIM][DMP]	292.135	0.321	1434.6	−0.619
[EMIM][Ac]	149.38	0.497	1119.6	−0.674
[EMIM][DEP]	348.016	0.607	1314.2	−0.576
[EMIM][EtSO4]	242.318	0.472	1259.5	−0.680

agree well with the measured pressures.

As for the ATES cycle model, due to a lack of studies on the ATES using IL-based working fluids, the experimental data of an ATES using H_2O/LiBr [22] is used for model validation. Fig. 3 shows the heat duties of the generator and condenser in the charging process, as well as the heat duties of the absorber and evaporator in the charging process. The calculated variation trends of heat duties agree well with the measured results. The minor deviations are mainly caused by heat and pressure losses of the experiments, which can be minimized by better insulation and design. It is worth noticing that the dynamic behaviors may differ from the simulation results in Section 3, which are mainly caused by different external water temperatures (fluctuated in experiment) and initial conditions.

It is concluded that the property model and the cycle model can be used to predict the ATES performance with high accuracies.

3. Charging and discharging characteristics of different H_2O/IL mixtures

The dynamic charging and discharging characteristics of the ATES system are compared among the four H_2O/IL mixtures, after which the cycle performance of the whole processes is obtained. The design parameters and operating conditions are as follows:

- The UA values of heat exchangers are $UA_g = UA_a = 4.4 \, \text{kW/}^\circ\text{C}$, $UA_c = UA_e = 3.2 \, \text{kW/}^\circ\text{C}$.
- The temperatures of the external heat source/sink are $t_{gi} = 95\,^\circ\text{C}$, $t_{ai} = t_{ci} = 35\,^\circ\text{C}$, $t_{ei} = 12\,^\circ\text{C}$.
- The mass flow rates of the external heat source/sink are $m_g = m_a = 1.2 \, \text{kg/s}$, $m_c = m_e = 0.8 \, \text{kg/s}$.
- The initial masses of the solution and refrigerant are $m_s = 200 \, \text{kg}$, $m_r = 0 \, \text{kg}$.

The above UA values are determined based on a design cooling capacity of 10 kW with temperature differences of 5 °C and 2 °C at the two ends of heat exchangers. Although the transient cooling capacity and temperature difference changes with time, we aim to achieve an average cooling capacity of 10 kW under the design temperature difference. Given the cooling capacity and temperature difference, the UA values of the generator/absorber and condenser/evaporator are designed. In addition, the above mass flow rates are determined with temperature changes of 3 °C though the heat exchangers.

The charging and discharging processes finish when the temperature differences between the external fluid inlet and the inside solution are smaller than 0.5 °C. The initial solution concentration of the charging process is the ending solution concentration of the discharging process.

3.1. Charging characteristics

The instantaneous heat input and heat rejection rates for the four H_2O/IL mixtures are compared in Fig. 4. For each mixture, the heat input (q_g) decreases as the charging process goes on, rapidly in the first 5 min and slowly later (Fig. 4(a)). The decrease of heat input
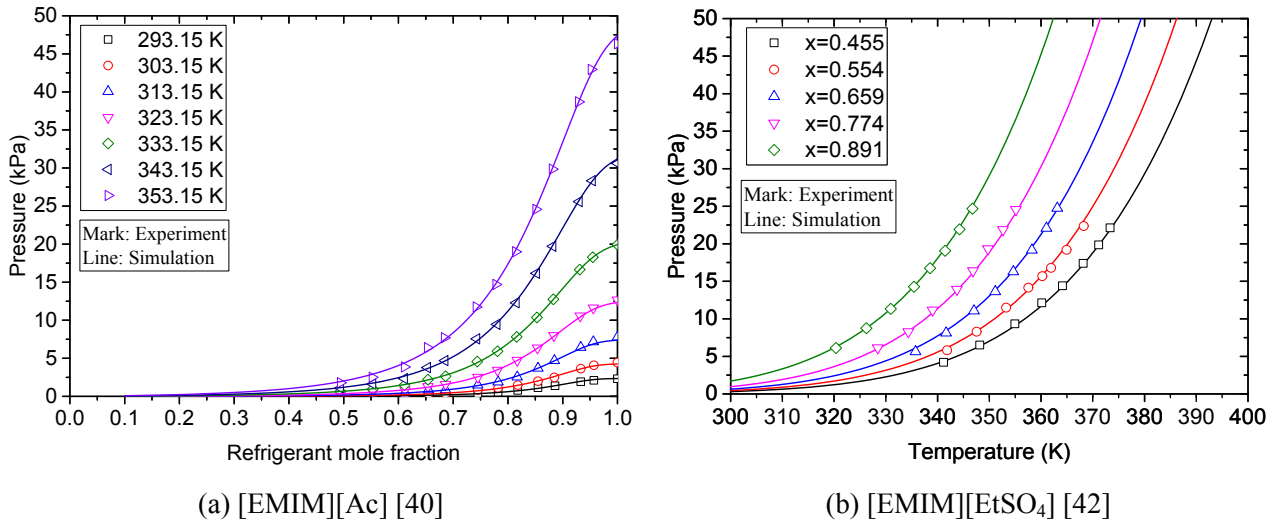
(a) [EMIM][Ac] [40]   (b) [EMIM][EtSO$_4$] [42]

Fig. 2. Comparisons between calculation and measurement of H$_2$O/IL mixtures.

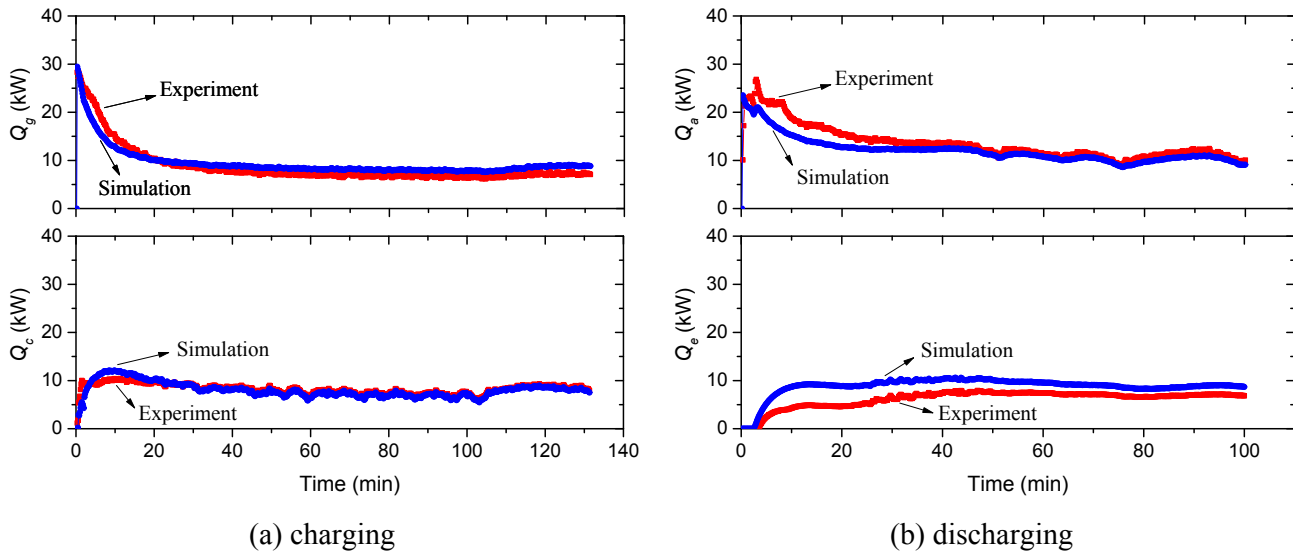(a) charging   (b) discharging

Fig. 3. Comparisons between calculation and measurement of ATES using H$_2$O/LiBr.

is caused by the increasing solution temperature and thus decreasing temperature difference. At the beginning, there is no vapor generation and only sensible heat transfer, so the solution temperature increases rapidly (Fig. 5(a)). After vapor generation occurs and latent heat transfer involves, the solution temperature increases slowly. Comparing different H$_2$O/IL mixtures, H$_2$O/[EMIM][Ac] generally has the highest charging rate while H$_2$O/[DMIM][DMP] has the lowest charging rate. H$_2$O/[EMIM][Ac] has the longest charging time while H$_2$O/[EMIM][EtSO$_4$] has the shortest charging time.

For each mixture, the heat rejection (q_c) is 0 at the beginning, increases rapidly then and decreases slowly later as the charging process goes on (Fig. 4(b)). At the beginning, there is no vapor generation and the vapor mass flow rate is 0 (Fig. 6(a)), thus there is no refrigerant condensation in the refrigerant tank. After vapor generation and condensation occur, vapor mass flow rate increases and the heat rejection increases rapidly. As the refrigerant fraction decreases (Fig. 5(b)), the generation weakens so that the generated vapor mass flow rate decreases. Consequently, the refrigerant

condensation weakens and the heat rejection decreases. Comparing different H$_2$O/IL mixtures, H$_2$O/[EMIM][EtSO$_4$] has the highest rejection rate in the first 30 min while H$_2$O/[EMIM][Ac] has the highest rejection rate after 30 min.

Fig. 5 shows the solution temperature and solution concentration while Fig. 6 shows the refrigerant flow rate and refrigerant pressure, which have been used to explain the dynamic characteristics of the thermal energy capacities in the charging process (Fig. 4). Fig. 5(b) indicates that H$_2$O/[EMIM][Ac] has the highest refrigerant fraction, which also decreases much slower with time. H$_2$O/[EMIM][EtSO$_4$] has the lowest refrigerant fraction, which also decreases much faster with time. These are mainly determined by the solubility differences among the ILs. Similar to the heat rejection, the refrigerant pressure does not change at the beginning, increases rapidly then and decreases slowly later as the charging process goes on (Fig. 6(b)). The pressure corresponds to the condensation temperature, which is determined by the heat transfer. A higher heat transfer rate leads to a larger temperature difference and thus a higher condensation temperature.
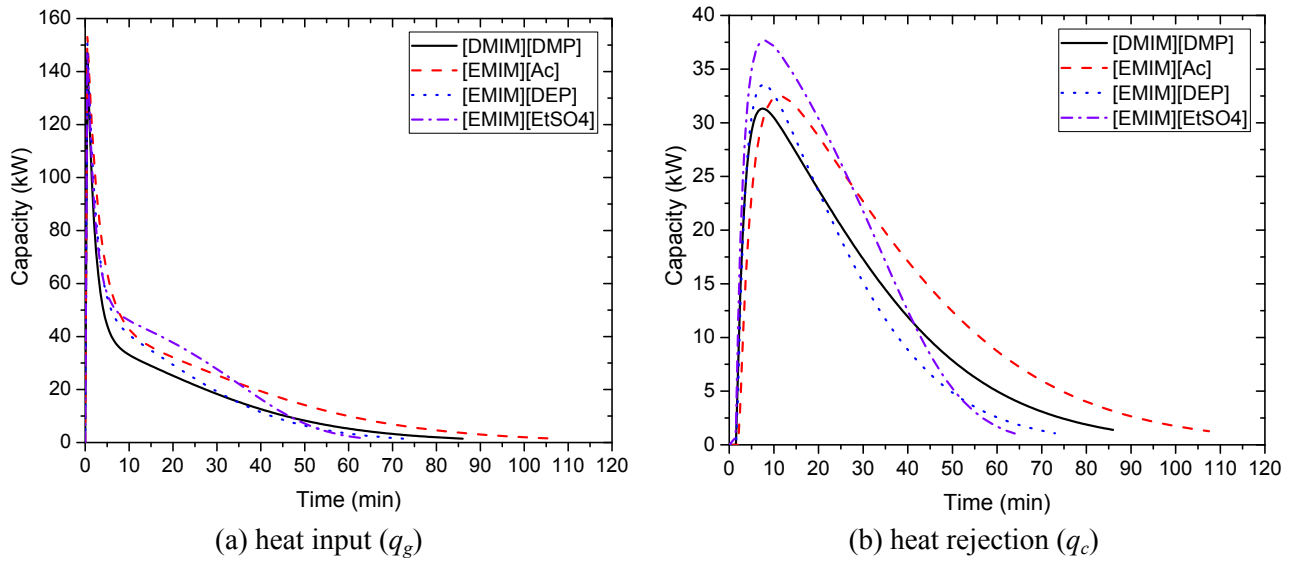
(a) heat input (q_g)

(b) heat rejection (q_c)

Fig. 4. Thermal energy capacities of charging process.

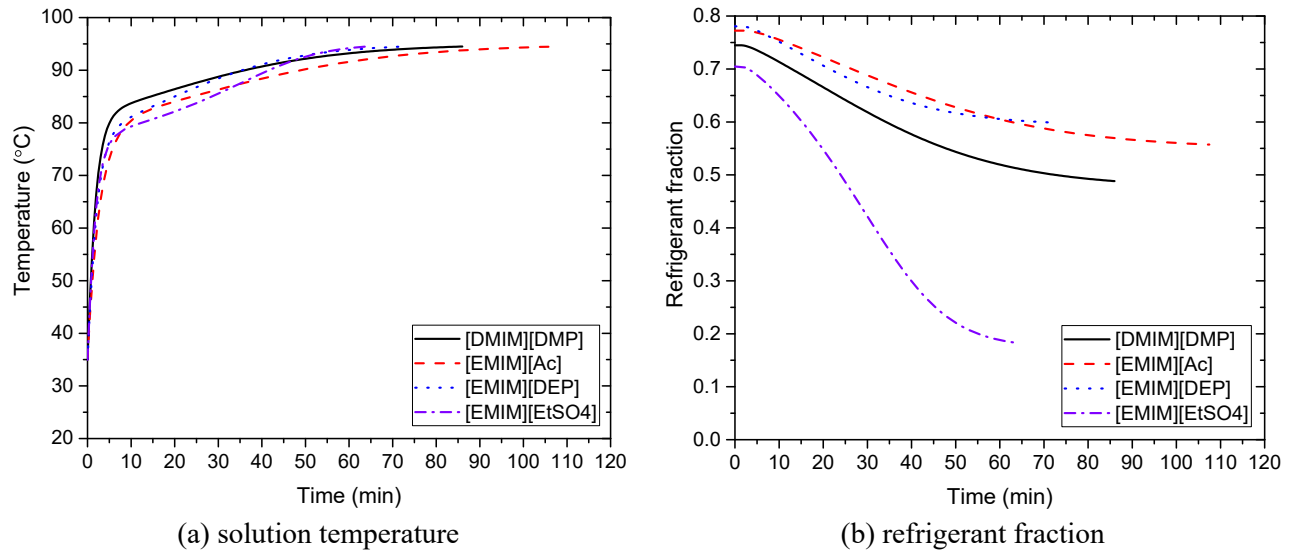

(a) solution temperature

(b) refrigerant fraction

Fig. 5. Solution parameters of charging process.

Figs. 7 and 8 present the liquid masses in the tanks and the outlet temperatures of the heat exchangers. The dynamic behaviors of these parameters are determined by the refrigerant mass flow rate and the heat duties. With vapor generation during the charging process, the solution mass gets lower while the refrigerant mass gets higher (Fig. 7). The variation rates depend on the vapor generation rate. The generator outlet temperature keeps increasing (Fig. 8(a)) since the heat input keeps decreasing (the temperature drop keeps decreasing) (Fig. 4(a)). Similar to the heat rejection, the condenser outlet temperature does not change at the beginning, increases rapidly then and decreases slowly later as the charging process goes on (Fig. 8(b)). This is because the variation of heat rejection is directly reflected by the variation of temperature rise of the cooling water.

3.2. Discharging characteristics

The instantaneous heat rejection rates and cooling capacity of

the four H_2O/IL mixtures are compared in Fig. 9. For each mixture, the heat rejection (q_a) decreases as the discharging process goes on, rapidly in the first 10 min and slowly later (Fig. 9(a)). The decrease of heat rejection is caused by the decreasing solution temperature and thus decreasing temperature difference. At the beginning, there is no vapor absorption and only sensible heat transfer, so the solution temperature decreases rapidly (Fig. 10(a)). After vapor absorption occurs and latent heat transfer involves, the solution temperature decreases slowly.

The cooling capacity (q_e) is 0 at the beginning (about 2 min), increases rapidly then and decreases slowly later as the discharging process goes on (Fig. 9(b)). At the beginning, there is no vapor absorption and the vapor mass flow rate is 0 (Fig. 11(a)), indicating that there is no refrigerant evaporation in the refrigerant tank. After vapor absorption and evaporation occur, vapor mass flow rate increases and the cooling capacity increases rapidly. As the refrigerant fraction increases (Fig. 10(b)), the absorption weakens so that the absorbed vapor mass flow rate decreases. Consequently, the
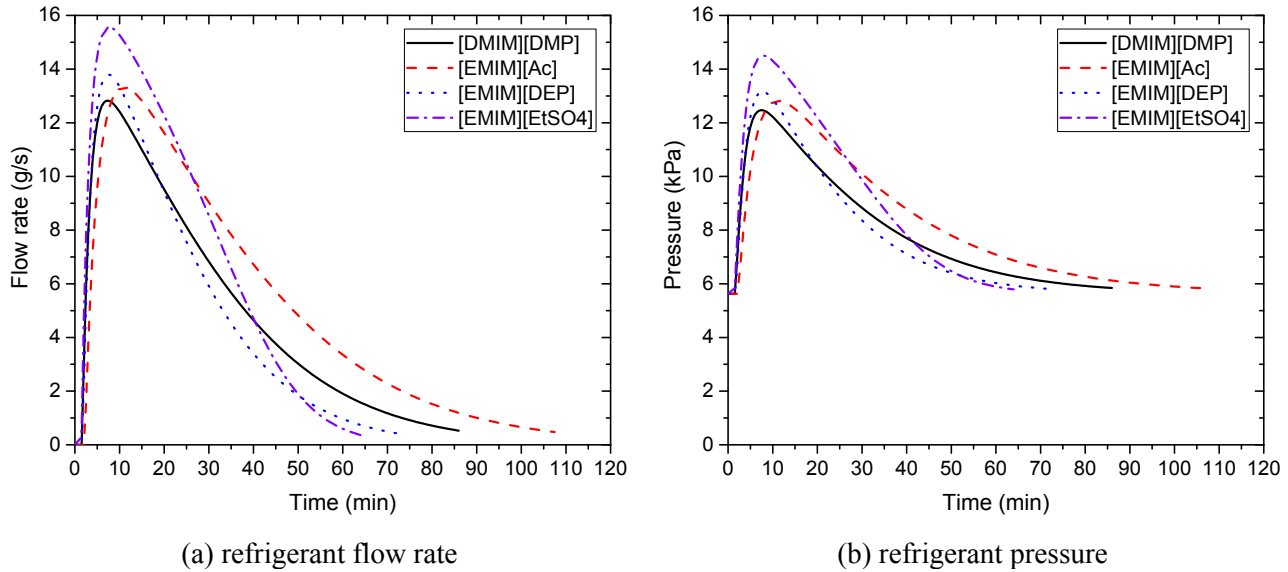
(a) refrigerant flow rate

(b) refrigerant pressure

Fig. 6. Refrigerant flow rate and pressure of charging process.

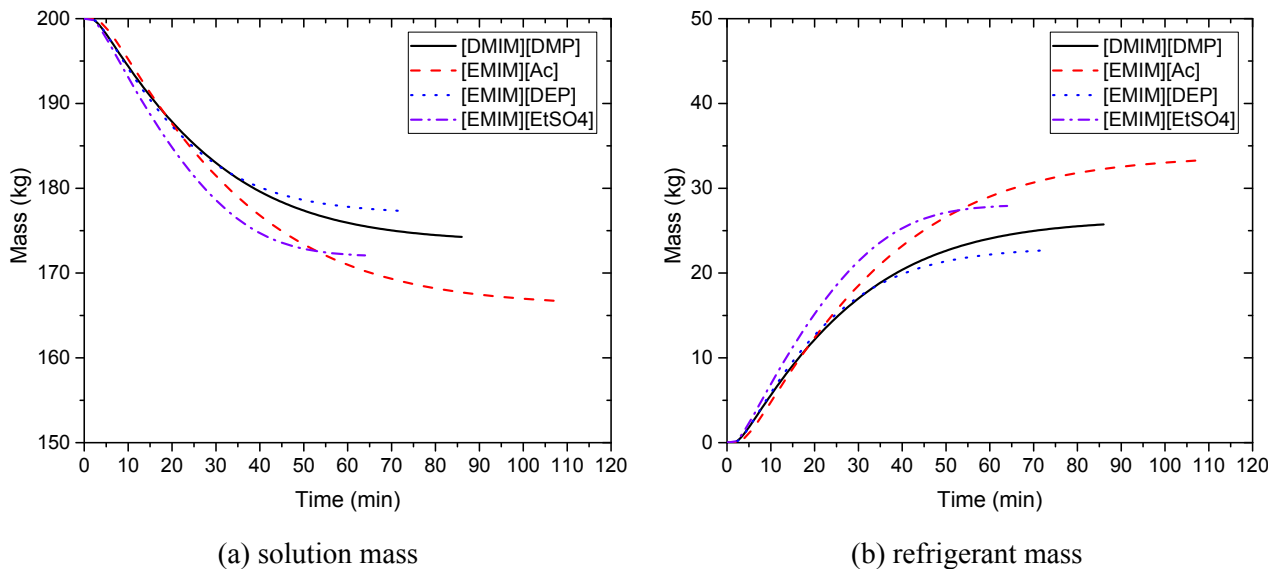(a) solution mass

(b) refrigerant mass

Fig. 7. Working fluid masses of charging process.

refrigerant evaporation decreases and the cooling capacity decreases.

Comparing different H_2O/IL mixtures, H_2O/[EMIM][Ac] generally has the highest discharging rate, while H_2O/[EMIM][EtSO$_4$] has the lowest discharging rate in the first 30 min and H_2O/[EMIM][DEP] has the lowest discharging rate after 30 min H_2O/[EMIM][EtSO$_4$] has the longest discharging time, with H_2O/[EMIM][Ac] being about 10 min shorter, while H_2O/[EMIM][DEP] has the shortest discharging time.

Figs. 10 and 11 show the solution temperature, solution concentration, refrigerant flow rate and refrigerant pressure, which have been used to explain the dynamic characteristics of the thermal energy capacities in the discharging process (Fig. 9). Fig. 10(b) indicates that H_2O/[EMIM][DEP] has the highest refrigerant fraction, which also increases much slower with time. H_2O/[EMIM][EtSO$_4$] has the lowest refrigerant fraction, which also increases much faster with time. Fig. 11(b) indicates that the

refrigerant pressure does not change at the beginning, decreases rapidly then and increases slowly later as the discharging process goes on. The pressure corresponds to the evaporation temperature, which is determined by the heat transfer. A higher heat transfer rate leads to a larger temperature difference and thus a lower evaporation temperature.

Figs. 12 and 13 present the liquid masses in the tanks and the outlet temperatures of the heat exchangers, which are determined by the refrigerant flow rate and heat duties. With vapor absorption during the discharging process, the solution mass gets higher while the refrigerant mass gets lower (Fig. 12). The variation rates depend on the vapor absorption rate. The absorber outlet temperature keeps decreasing (Fig. 13(a)) since the heat rejection keeps decreasing (the temperature rise keeps decreasing). Corresponding to the cooling capacity, the evaporator outlet temperature does not change at the beginning (about 2 min), decreases rapidly then and increases slowly later as the discharging process goes on
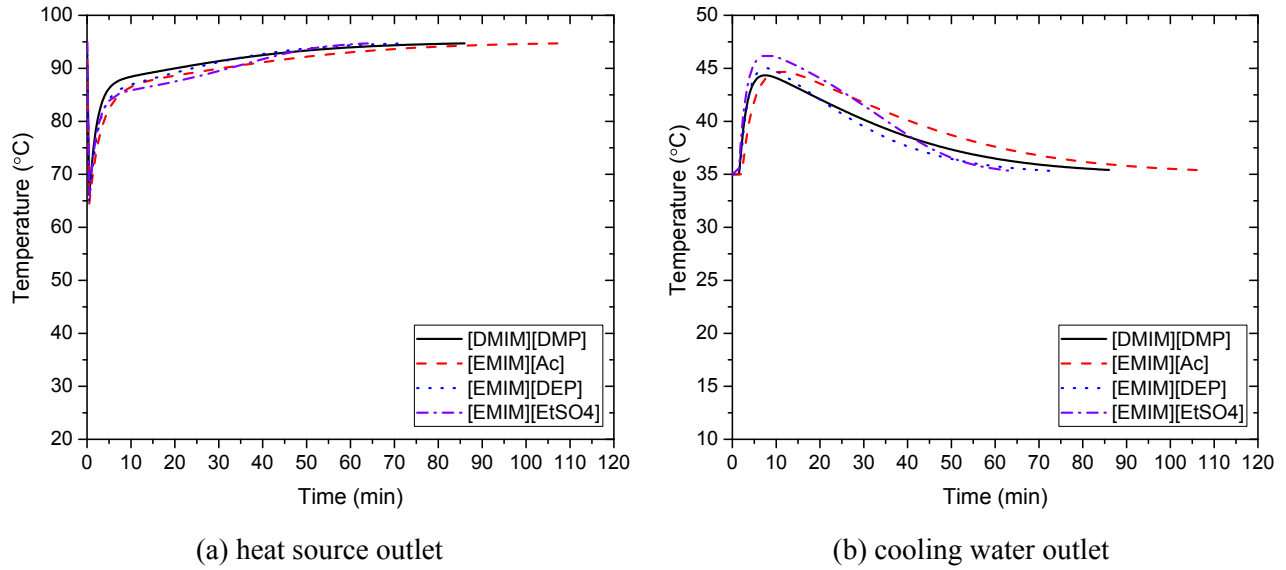
(a) heat source outlet

(b) cooling water outlet

Fig. 8. External water temperatures of charging process.

(a) heat rejection
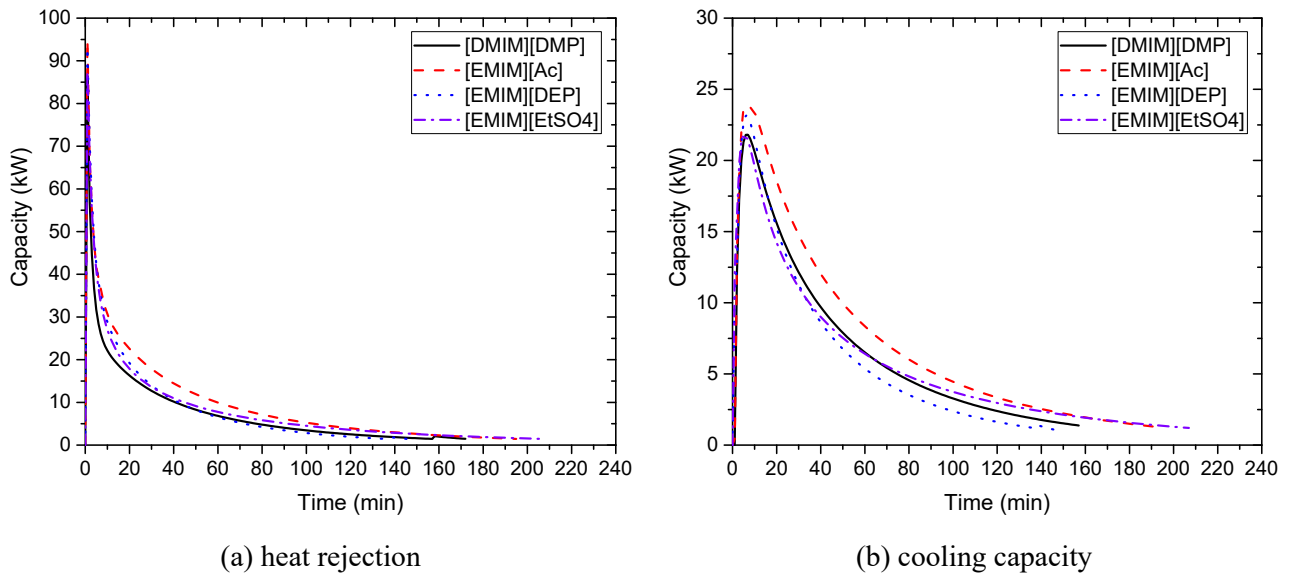
(b) cooling capacity

Fig. 9. Thermal energy capacities of discharging process.

(Fig. 13(b)). This is because the variation of cooling capacity is directly reflected by the variation of temperature drop of the chilled water.

3.3. ATES cycle performance

Based on the dynamic characteristics of the charging and discharging processes, the cycle performance is derived by integrating the instantaneous parameters. Table 4 summarizes the heat duties, COP, ESD, charging time and discharging time of the four H_2O/IL mixtures. The charged thermal energy is in the order of: [EMIM][Ac] > [EMIM][EtSO4] > [EMIM][DEP] > [DMIM][DMP]. The discharged cold energy is in the order of: [EMIM][Ac] > [EMIM][EtSO4] > [DMIM][DMP] > [EMIM][DEP]. As a result, [DMIM][DMP] yields the highest COP of 0.722 while [EMIM][DEP] yields the lowest COP of 0.603. [DMIM][DMP] shows the highest ESD of 94.1 kW h/m^3 while [EMIM][DEP] shows the lowest ESD of 77.5 kW h/m^3. In addition, [EMIM][Ac] needs 107.5 min to fully charge the thermal energy, while [EMIM][EtSO4] only needs 64.0 min [EMIM][EtSO4] needs 207.0 min to fully discharge the cold energy, while [EMIM][DEP] only needs 146.0 min. The discharging process takes much longer time than the discharging process.

Considering that the charged/discharged energy and charging/discharging time differ a lot among the working fluids. The average charging rate (total charged heat over total charging time) and the average discharging rate (total discharged cold over total discharging time) are used to compare the energy intensity of charging/discharging. It is found that [EMIM][EtSO4] has the highest average charging rate of 0.469 kW h/min while [DMIM][DMP] has the lowest of 0.286 kW h/min. In addition, [EMIM][Ac] has the highest average discharging rate of 0.118 kW h/min while [EMIM][EtSO4] has the lowest of 0.093 kW h/min.
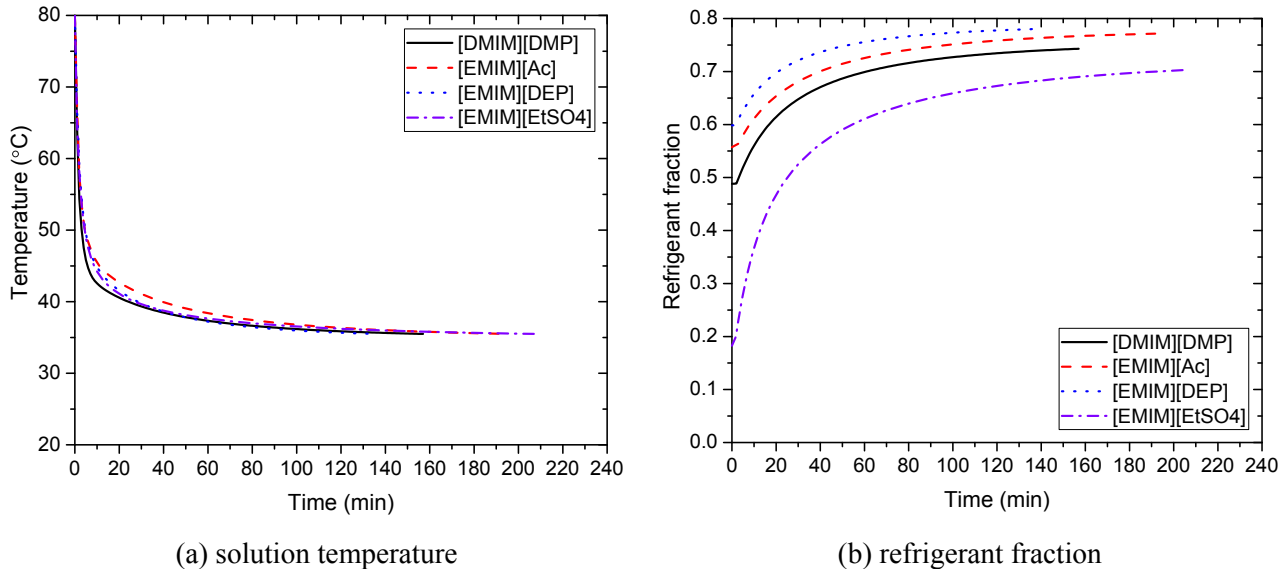
(a) solution temperature

(b) refrigerant fraction

Fig. 10. Solution parameters of discharging process.

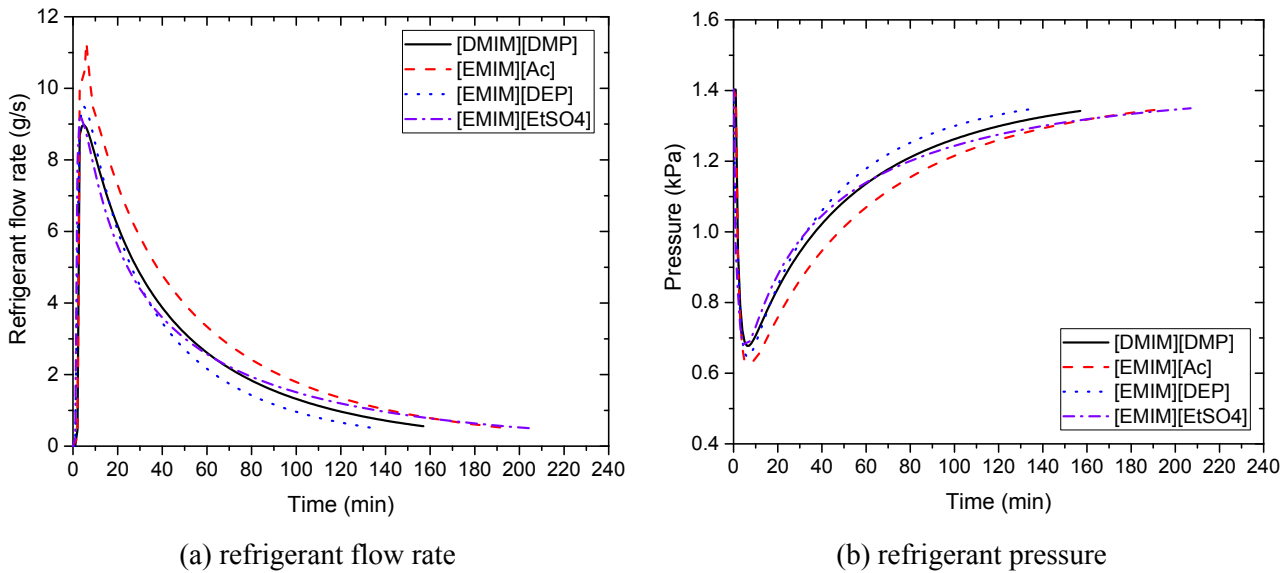(a) refrigerant flow rate

(b) refrigerant pressure

Fig. 11. Refrigerant flow rate and pressure of discharging process.

4. Characteristics of selected H_2O/IL mixture under various operating conditions

The comparisons among different H_2O/IL mixtures reveal that H_2O/[DMIM][DMP] has the highest COP and ESD, so it is further analyzed under various operating conditions. When changing one operating parameters, other parameters are kept unchanged.

4.1. Effect of charging temperature

The charging and discharging characteristics under various charging temperatures ($t_{gi} = 80, 90, 95$ and $100\,°C$) are presented in Figs. 14 and 15. The dynamic variation trends are similar under different charging temperatures. As the charging temperature increases, the heat input rate increases and the charging time decreases (Fig. 14(a)). This is because a higher charging temperature accelerates the vapor generation, leading to more rapid reduction

of refrigerant fraction in the solution (Fig. 14 (b)). Fig. 15(a) shows that the discharged cooling capacity increases as the charging temperature increases, due to the more concentrated solution at the end of the charging process (Fig. 14(b)) and the beginning of the discharging process (Fig. 15(b)). The more concentrated solution also leads to increased discharging time.

Based on the dynamic characteristics, the cycle performance is summarized in Table 5. As the charging temperature ranges from $85\,°C$ to $100\,°C$, the charged thermal energy increases from $20.0\,kW\,h$ to $26.5\,kW\,h$, the discharged cold energy increases from $14.2\,kW\,h$ to $19.1\,kW\,h$. The COP first increases from 0.709 to 0.722 and then decreases to 0.721. The ESD increases from $77.3\,kW\,h/m^3$ to $100.2\,kW\,h/m^3$. In addition, the charging time decreases from $95.5\,min$ to $81.5\,min$, corresponding to an average charging rate from $0.209\,kW\,h/min$ to $0.325\,kW\,h/min$. The discharging time increases from $148.0\,min$ to $159.0\,min$, corresponding to an average discharging rate from $0.096\,kW\,h/min$ to $0.120\,kW\,h/min$.
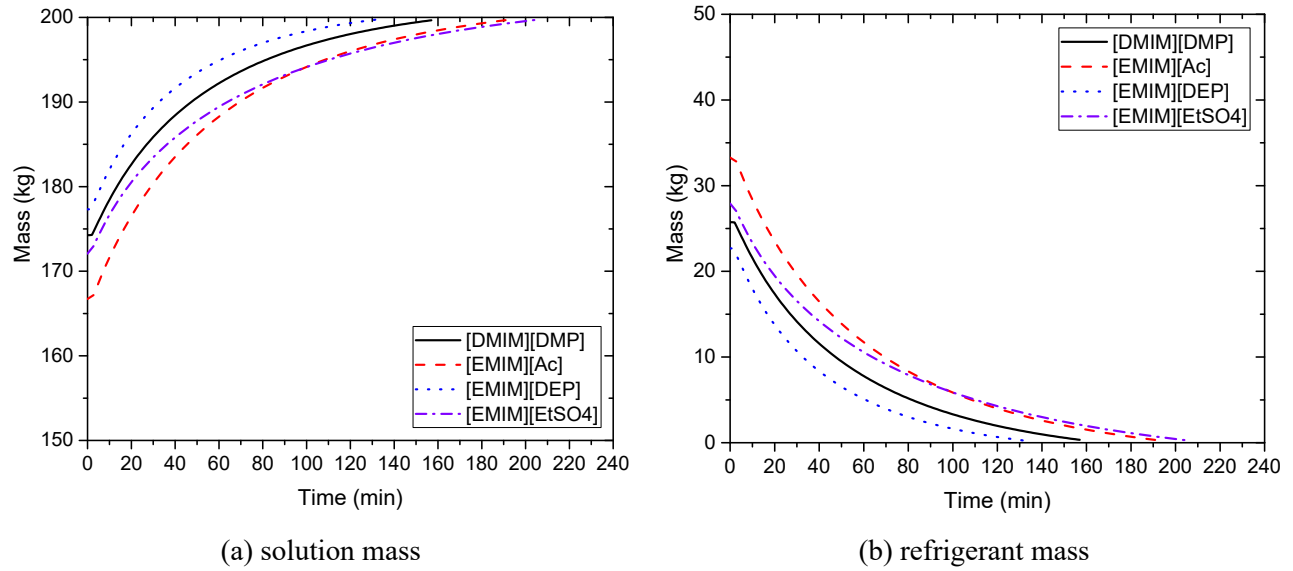
(a) solution mass

(b) refrigerant mass

Fig. 12. Working fluid masses of discharging process.

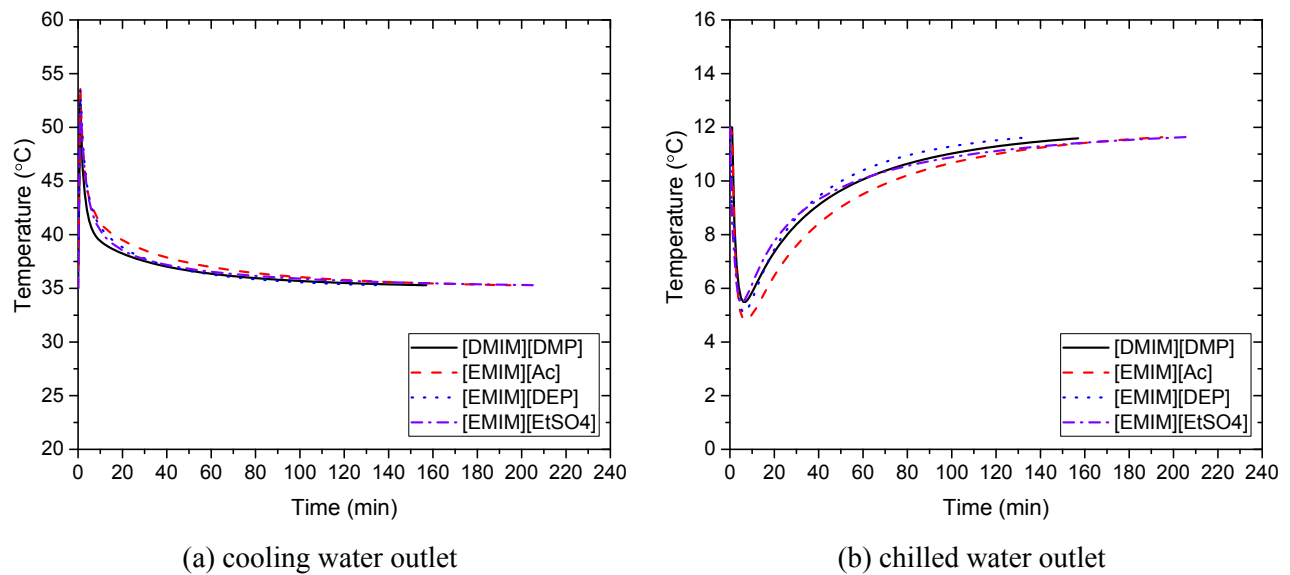(a) cooling water outlet

(b) chilled water outlet

Fig. 13. External water temperatures of discharging process.

Table 4
Cycle performance of the ATES using different H_2O/IL mixtures.

Index	[DMIM][DMP]	[EMIM][Ac]	[EMIM][DEP]	[EMIM][EtSO$_4$]
Q_g (kWh)	24.6	35.2	26.1	30.0
Q_c (kWh)	18.0	23.2	15.8	19.4
Q_a (kWh)	21.8	31.6	23.3	27.3
Q_e (kWh)	17.7	22.9	15.7	19.3
COP	0.722	0.652	0.603	0.644
ESD (kWh/m^3)	94.1	92.6	77.5	87.8
Charging time (min)	86.0	107.5	73.0	64.0
Discharging time (min)	172.0	195.0	146.0	207.0
Average charging rate (kWh/min)	0.286	0.327	0.358	0.469
Average discharging rate (kWh/min)	0.103	0.118	0.108	0.093

(a) heat input

(b) refrigerant fraction

Fig. 14. Effect of charging temperature on charging process.
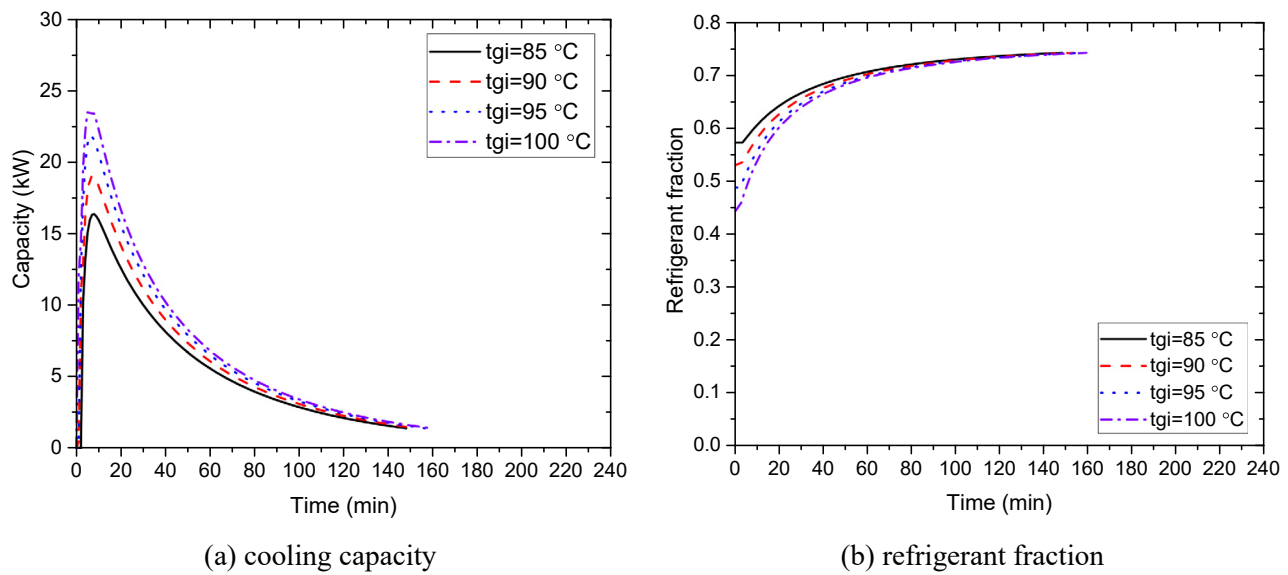

(a) cooling capacity

(b) refrigerant fraction
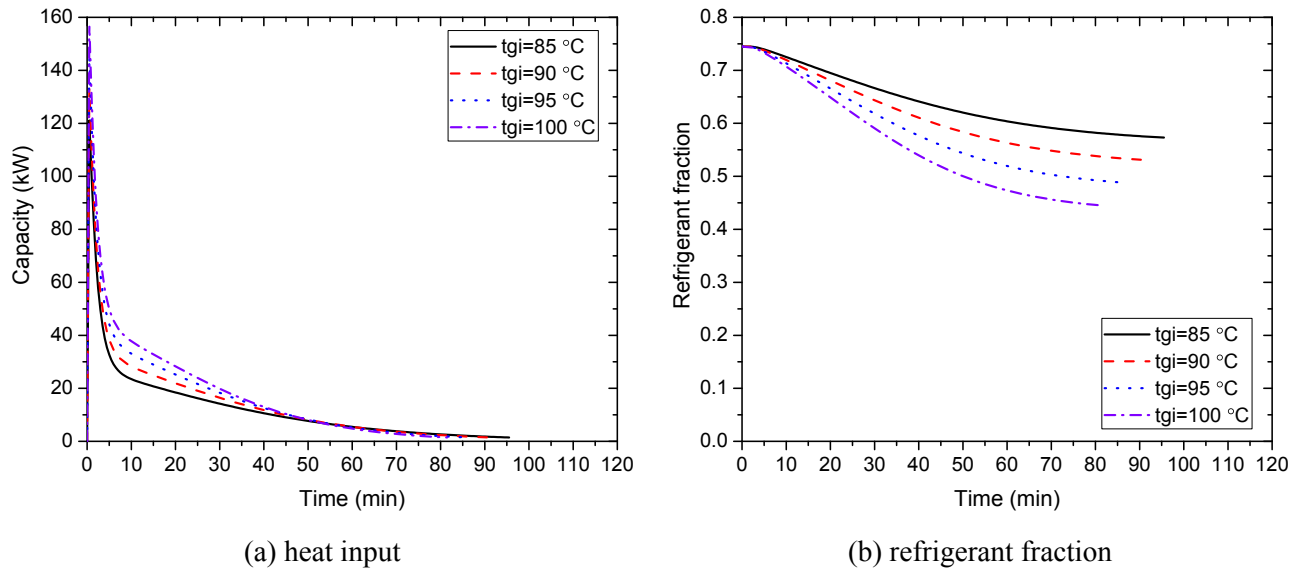
Fig. 15. Effect of charging temperature on discharging process.

Table 5
Cycle performance of the H_2O/[DMIM][DMP] ATES under various charging temperatures.

Index	$t_{gi} = 85\,°C$	$t_{gi} = 90\,°C$	$t_{gi} = 95\,°C$	$t_{gi} = 100\,°C$
Q_g (kWh)	20.0	22.4	24.6	26.5
Q_c (kWh)	14.3	16.3	18.0	19.4
Q_a (kWh)	18.5	20.3	21.8	23.2
Q_e (kWh)	14.2	16.1	17.7	19.1
COP	0.709	0.718	0.722	0.721
ESD (kWh/m^3)	77.3	86.5	94.1	100.2
Charging time (min)	95.5	91.0	86.0	81.5
Discharging time (min)	148.0	153.0	157.0	159.0
Average charging rate (kWh/min)	0.209	0.246	0.286	0.325
Average discharging rate (kWh/min)	0.096	0.105	0.113	0.120

(a) heat input

(b) refrigerant fraction
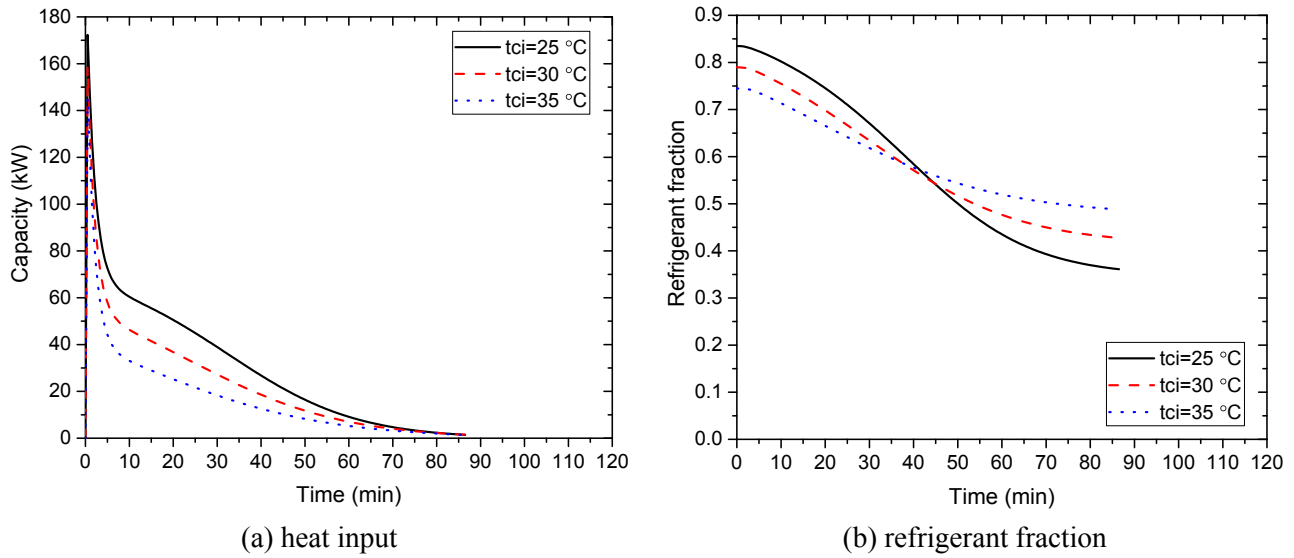
Fig. 16. Effect of cooling water temperature on charging process.
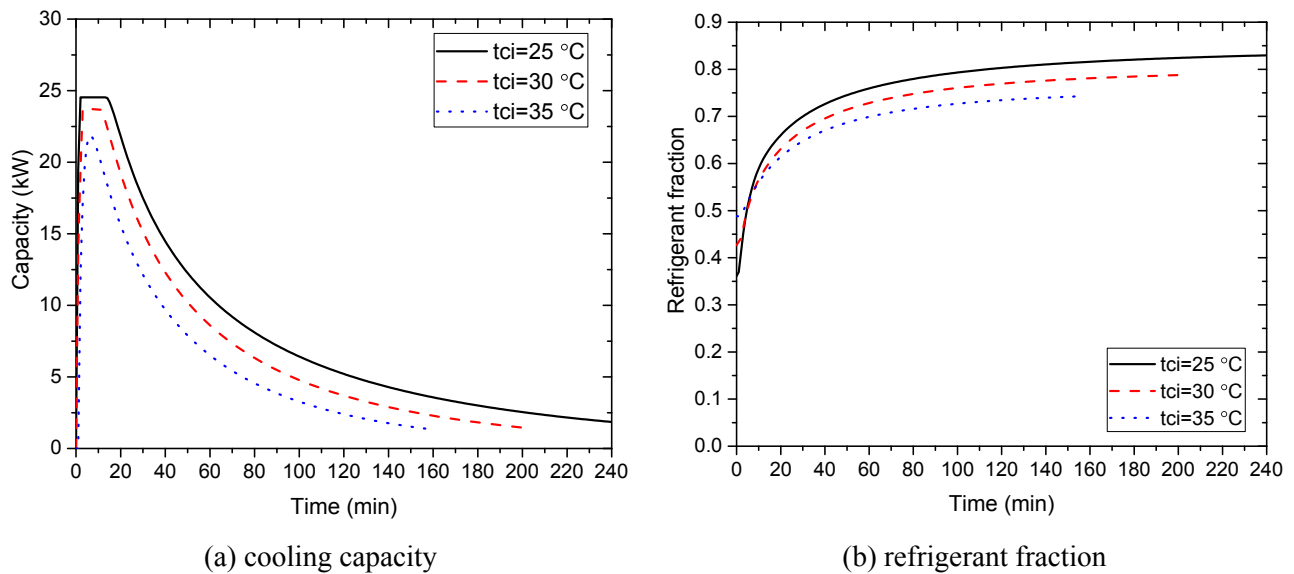

(a) cooling capacity

(b) refrigerant fraction

Fig. 17. Effect of cooling water temperature on discharging process.

4.2. Effect of cooling water temperature

The charging and discharging characteristics under various cooling water temperatures ($t_{ci} = 25$, 30 and 35 °C) are presented in Figs. 16 and 17. As the cooling water temperature increases, the heat input rate decreases (Fig. 16(a)). On the one hand, a higher cooling temperature rises the charging pressure and thus decelerates the vapor generation, indicated by the more slowly reduction of refrigerant fraction (Fig. 16 (b)). On the other hand, a higher cooling temperature worsens the vapor absorption in the discharging process and in turn worsens the vapor generation in the charging process. The discharged cooling capacity decreases (Fig. 17(a)) due to the less concentrated solution at the end of the charging process (Fig. 16(b)) and the beginning of the discharging process (Fig. 17(b)).

Table 6
Cycle performance of the H_2O/[DMIM][DMP] ATES under various cooling water temperatures.

Index	$t_{ci} = 25$ °C	$t_{ci} = 30$ °C	$t_{ci} = 35$ °C
Q_g (kWh)	43.7	33.3	24.6
Q_c (kWh)	36.4	26.3	18.0
Q_a (kWh)	40.0	30.1	21.8
Q_e (kWh)	32.5	24.7	17.7
COP	0.744	0.741	0.722
ESD (kWh/m^3)	149.5	122.5	94.1
Charging time (min)	86.5	87.0	86.0
Discharging time (min)	240.0	204.0	157.0
Average charging rate (kWh/min)	0.505	0.383	0.286
Average discharging rate (kWh/min)	0.135	0.121	0.113

(a) heat input
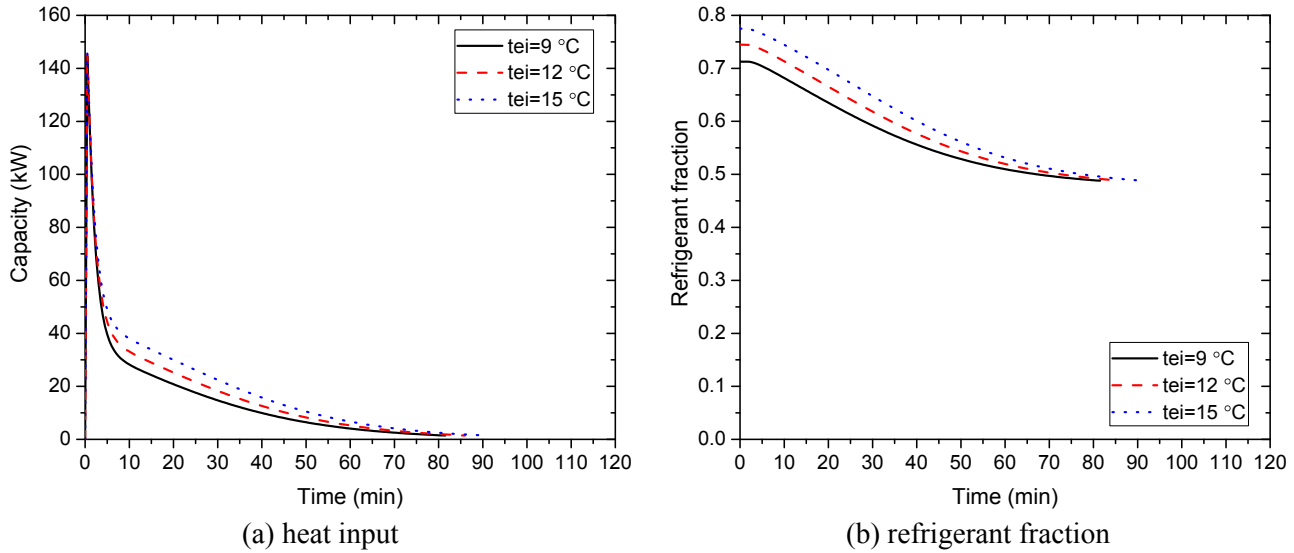
(b) refrigerant fraction

Fig. 18. Effect of discharging temperature on charging process.

The less concentrated solution also leads to decreased discharging time.

Based on the dynamic characteristics, the cycle performance is summarized in Table 6. The effect of cooling water temperature on the cycle performance is quite significant. As the cooling water temperature ranges from 25 °C to 35 °C, the charged thermal energy decreases from 43.7 kW h to 24.6 kW h, the discharged cold energy decreases from 32.5 kW h to 17.7 kW h. The COP decreases from 0.744 to 0.721, while the ESD decreases from 149.5 kW h/m^3 to 94.1 kW h/m^3. In addition, the charging time is relatively stable (about 87 min), with an average charging rate from 0.505 kW h/min to 0.286 kW h/min. The discharging time decreases from 240.0 min to 157.0 min, corresponding to an average discharging rate from 0.135 kW h/min to 0.113 kW h/min.

4.3. Effect of discharging temperature

The charging and discharging characteristics under various discharging temperatures (t_{ei} = 9, 12 and 15 °C) are presented in Figs. 18 and 19. As the discharging temperature increases, the heat input rate increases and the charging time also increases (Fig. 18(a)). This is because a higher discharging temperature rises the discharging pressure and thus strengthens the vapor absorption, leading to a higher refrigerant fraction at the end of the discharging process (Fig. 19(b)) and the beginning of the charging process (Fig. 18(b)). Fig. 19(a) shows that the discharged cooling capacity increases as the discharging temperature increases, due to the strengthened vapor absorption. The higher discharging pressure also prolongs the discharging time.

Based on the dynamic characteristics, the cycle performance is summarized in Table 7. As the discharging temperature ranges from
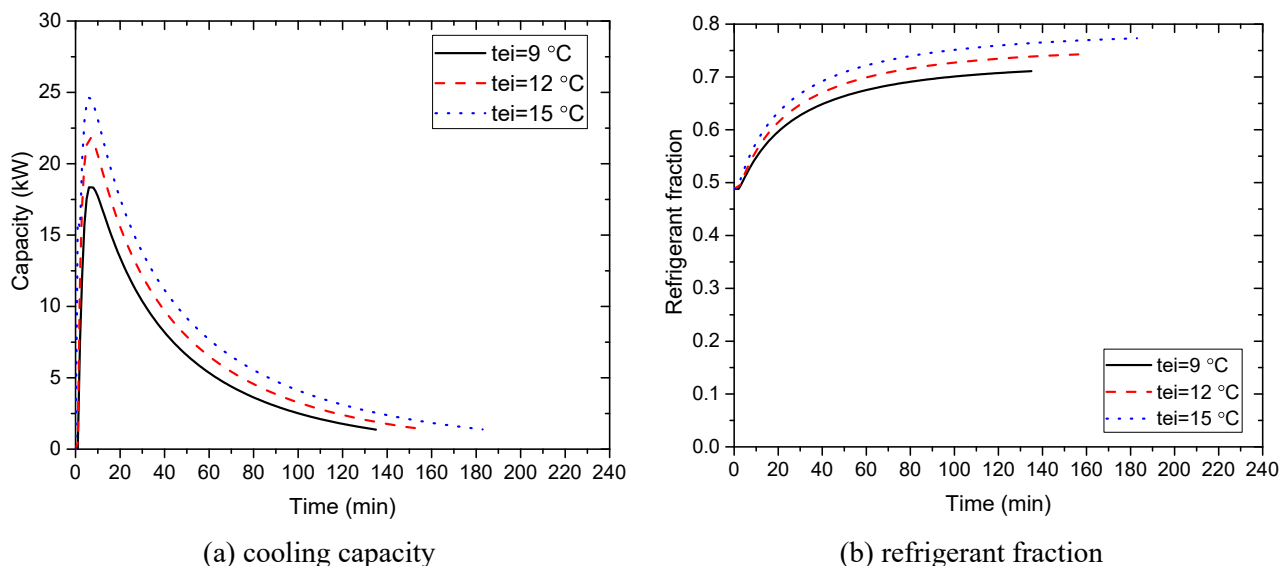

(a) cooling capacity

(b) refrigerant fraction

Fig. 19. Effect of discharging temperature on discharging process.

Table 7
Cycle performance of the H$_2$O/[DMIM][DMP] ATES under various discharging temperatures.

Index	$t_{ei}=9\,°C$	$t_{ei}=12\,°C$	$t_{ci}=15\,°C$
Q_g (kWh)	21.0	24.6	28.6
Q_c (kWh)	14.4	18.0	22.0
Q_a (kWh)	18.4	21.8	25.7
Q_e (kWh)	14.1	17.7	21.8
COP	0.675	0.722	0.761
ESD (kWh/m^3)	77.6	94.1	111.5
Charging time (min)	81.5	86.0	90.5
Discharging time (min)	135.0	157.0	183.0
Average charging rate (kWh/min)	0.258	0.286	0.316
Average discharging rate (kWh/min)	0.104	0.113	0.119

9 °C to 15 °C, the charged thermal energy increases from 21.0 kW h to 28.6 kW h, the discharged cold energy increases from 14.1 kW h to 21.8 kW h. The COP increases from 0.675 to 0.761, while the ESD increases from 77.6 kW h/m^3 to 111.5 kW h/m^3. In addition, the charging time increases from 81.5 min to 90.5 min, corresponding to an average charging rate from 0.258 kW h/min to 0.316 kW h/min. The discharging time increases from 135.0 min to 183.0 min, corresponding to an average discharging rate from 0.104 kW h/min to 0.119 kW h/min.

It is worth noticing that the working conditions in this study is not fully covered; with higher driving source temperatures and lower cooling water temperatures, the ESDs could be even higher while being free of crystallization. In addition, more ILs should be explored to further enhance the ESDs. Apart from crystallization and ESD, the COP is also an important index for the ATES systems. The cooling COP of H$_2$O/IL obtained in this work if quite high, which could be higher than that of H$_2$O/salt. As reported by Dong et al. [39], the H$_2$O/IL and H$_2$O/LiBr performed very closely in an absorption cooling cycle, but the H$_2$O/IL can relive the problem of crystallization and corrosion. This could be another driving force to explore ILs in ATES systems.

5. Conclusions

The ATES systems using H$_2$O/IL mixtures as novel working fluids are explored to avoid the crystallization problem. The NTRL property model and the dynamic cycle model are established and validated against experimental data. The charging/discharging characteristics and cycle performance are compared for four ILs ([DMIM][DMP], [EMIM][Ac], [EMIM][DEP], and [EMIM][EtSO$_4$]). The main conclusions are drawn as follows:

(1) Comparing various ILs in terms of the COP, ESD, charging/discharging time, charging/discharging power rate:
- [DMIM][DMP] yields the highest COP of 0.722 while [EMIM][DEP] yields the lowest COP of 0.603.
- [DMIM][DMP] shows the highest ESD of 94.1 kW h/m^3 while [EMIM][DEP] shows the lowest ESD of 77.5 kW h/m^3.
- [EMIM][Ac] needs the longest charging time of 107.5 min, while [EMIM][EtSO$_4$] needs the shortest of 64.0 min [EMIM][EtSO$_4$] needs the longest discharging time of 207.0 min while [EMIM][DEP] needs the shortest of 146.0 min.
- [EMIM][EtSO$_4$] has the highest average charging rate of 0.469 kW h/min while [DMIM][DMP] has the lowest of 0.286 kW h/min. [EMIM][Ac] has the highest average discharging rate of 0.118 kW h/min while [EMIM][EtSO$_4$] has the lowest of 0.093 kW h/min.
(2) The effects of different operating parameters on the performance of ATES using [DMIM][DMP] are summarized:
- As the charging temperature increases from 85 °C to 100 °C, the cooling capacity increases from 14.2 kW h to 19.1 kW h, the COP varies between 0.709 and 0.722, while the ESD increases from 77.3 kW h/m^3 to 100.2 kW h/m^3.
- As the cooling water temperature increases from 25 °C to 35 °C, the cooling capacity decreases from 32.5 kW h to 17.7 kW h, the COP decreases from 0.744 to 0.721, while the ESD decreases from 149.5 kW h/m^3 to 94.1 kW h/m^3.
- As the discharging temperature increases from 9 °C to 15 °C, the cooling capacity increases from 14.1 kW h to 21.8 kW h, the COP increases from 0.675 to 0.761, while the ESD increases from 77.6 kW h/m^3 to 111.5 kW h/m^3.

In summary, it is feasible to use H$_2$O/ILs as crystallization-free working fluids of the ATES systems. [DMIM][DMP] is the best-performing one in terms of high COP and ESD. The highest COP is 0.761 and the highest ESD is 149.5 kW h/m^3 in the investigated operating conditions. This study aims to provide theoretical references and suggestions for the selection of novel working fluids for the ATES systems. Future work includes comparisons with the conventional working fluids, regulation of the ATES system to accommodate the building cooling loads, as well as economic analysis considering initial cost and energy savings under various application scenarios.

Appendix

Fig. A1 shows the calculation algorithm for the ATES simulation based on the model developed in section 2.
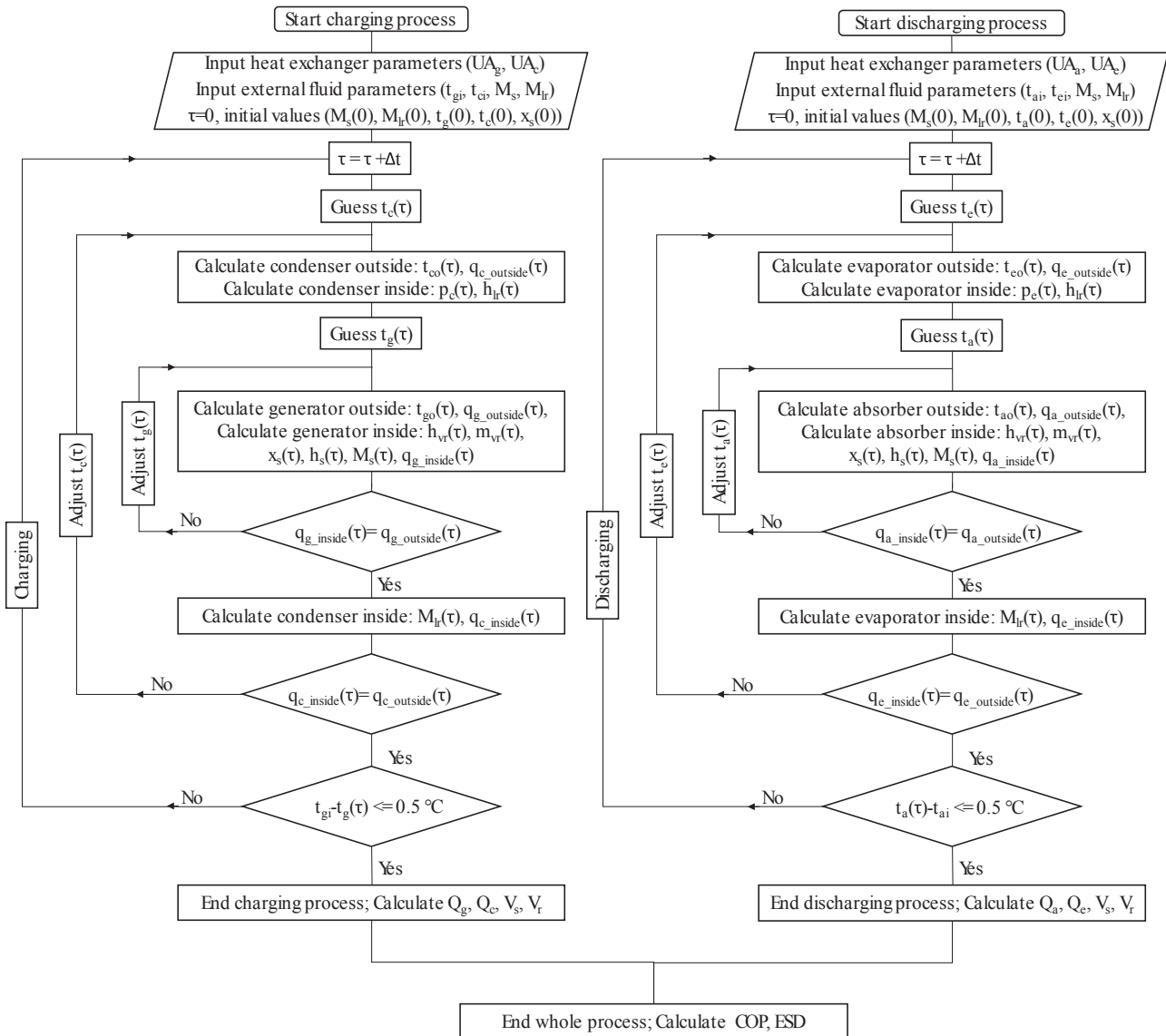

Fig. A1. Flow chart of the ATES simulation process.

References

[1] Li X, Wu W, Yu CW. Energy demand for hot water supply for indoor environments: problems and perspectives. 2015.
[2] International Energy Agency. The Future of Cooling: opportunities for energy efficient air conditioning. 2018.
[3] Li G, Hwang Y, Radermacher R, Chun HH. Review of cold storage materials for subzero applications. Energy 2013;51:1—17.
[4] Alva G, Lin Y, Fang G. An overview of thermal energy storage systems. Energy 2018;144:341—78.
[5] Yu N, Wang RZ, Wang LW. Sorption thermal storage for solar energy. Prog Energy Combust Sci 2013;39(5):489—514.
[6] Arteconi A, Ciarrocchi E, Pan Q, Carducci F, Comodi G, Polonara F, Wang R. Thermal energy storage coupled with PV panels for demand side management of industrial building cooling loads. Appl Energy 2017;185:1984—93.
[7] Rahdar MH, Emamzadeh A, Ataei A. A comparative study on PCM and ice thermal energy storage tank for air-conditioning systems in office buildings. Appl Therm Eng 2016;96:391—9.
[8] Sciacovelli A, Gagliardi F, Verda V. Maximization of performance of a PCM latent heat storage system with innovative fins. Appl Energy 2015;137:707—15.
[9] Hadorn J. Advanced storage concepts for active solar energy—IEA SHC Task 32. In: Eurosun — 1st international conference on solar heating, cooling and buildings; 2008.
[10] Zhang H, Baeyens J, Caceres G, Degreve J, Lv Y. Thermal energy storage: recent developments and practical aspects. Prog Energy Combust Sci 2016;53:1—40.
[11] N'tsoukpoe KE, Liu H, Le Pierrès N, Luo L. A review on long-term sorption solar energy storage. Renew Sustain Energy Rev 2009;13(9):2385—96.
[12] Ibrahim NI, Al-Sulaiman FA, Ani FN. Performance characteristics of a solar driven lithium bromide-water absorption chiller integrated with absorption energy storage. Energy Convers Manag 2017;150:188—200.
[13] Le Pierrès N, Huaylla F, Stutz B, Perraud J. Long-term solar heat storage process by absorption with the KCOOH/H2O couple: experimental investigation. Energy 2017;141:1313—23.
[14] Perier-Muzet M, Le Pierres N. Modeling and analysis of energetic and exergetic efficiencies of a LiBr/H 2 0 absorption heat storage system for solar space heating in buildings. Energy Effic. 2016;9(2):281—99.

[15] Wu W, Wang B, Shi W, Li X. An overview of ammonia-based absorption chillers and heat pumps. Renew Sustain Energy Rev 2014;31:681−707.

[16] Wu W, Wang B, Shi W, Li X. Absorption heating technologies: a review and perspective. Appl Energy 2014;130:51−71.

[17] Wu W, Zhang H, You T, Li X. Performance comparison of absorption heating cycles using various low-GWP and natural refrigerants. Int J Refrig 2017;82: 56−70.

[18] Weber R, Dorer V. Long-term heat storage with NaOH. Vacuum 2008;82(7): 708−16.

[19] Xu SM, Huang XD, Du R. An investigation of the solar powered absorption refrigeration system with advanced energy storage technology. Sol Energy 2011;85(9):1794−804.

[20] El-Shaarawi MAI, Said SAM, Siddiqui FR. Unsteady thermodynamic analysis for a solar driven dual storage absorption refrigeration cycle in Saudi Arabia. Sol Energy 2014;110:286−302.

[21] El-Shaarawi MAI, Al-Ugla AA. Unsteady analysis for solar-powered hybrid storage LiBr-water absorption air-conditioning. Sol Energy 2017;144:556−68.

[22] Zhang X, Li M, Shi W, Wang B, Li X. Experimental investigation on charging and discharging performance of absorption thermal energy storage system. Energy Convers Manag 2014;85:425−34.

[23] Fumey B, Weber R, Gantenbein P, Daguenet-Frick X, Stoller S, Fricker R, Dorer V. Operation results of a closed sorption heat storage prototype. Energy Procedia 2015;73:324−30.

[24] Zhao T, Min Y, Chen Q, Hao JH. Electrical circuit analogy for analysis and optimization of absorption energy storage systems. Energy 2016;104:171−83.

[25] Mugnier D, Goetz V. Energy storage comparison of sorption systems for cooling and refrigeration. Sol Energy 2001;71(1):47−55.

[26] Hui L, N'Tsoukpoe KE, Lingai L. Evaluation of a seasonal storage system of solar energy for house heating using different absorption couples. Energy Convers Manag 2011;52(6):2427−36.

[27] N'tsoukpoe KE, Perier-Muzet M, Le Pierrès N, Luo L, Mangin D. Thermodynamic study of a LiBr-H2O absorption process for solar heat storage with crystallisation of the solution. Sol Energy 2014;104:2−15.

[28] Lefebvre E, Fan L, Gagnière E, Bennici S, Auroux A, Mangin D. Lithium bromide crystallization in water applied to an inter-seasonal heat storage process. Chem Eng Sci 2015;133:2−8.

[29] Rosato A, Sibilio S. Preliminary experimental characterization of a three-phase absorption heat pump. Int J Refrig 2013;36(3):717−29.

[30] Yu N, Wang RZ, Lu ZS, Wang LW, Ishugah TF. Evaluation of a three-phase sorption cycle for thermal energy storage. Energy 2014;67:468−78.

[31] Zheng D, Dong L, Huang W, Wu X, Nie N. A review of imidazolium ionic liquids research and development towards working pair of absorption cycle. Renew Sustain Energy Rev 2014;37:47−68.

[32] Kim S, Patel N, Kohl PA. Performance simulation of ionic liquid and hydrofluorocarbon working fluids for an absorption refrigeration system. Ind Eng Chem Res 2013;52(19):6329−35.

[33] Cera-Manjarres A, Salavera D, Coronas A. Vapour pressure measurements of ammonia/ionic liquids mixtures as suitable alternative working fluids for absorption refrigeration technology. Fluid Phase Equilib 2018;476(B):48−60. 25.

[34] Wu W, You T, Zhang H, Li X. Comparisons of different ionic liquids combined with trans-1, 3, 3, 3-tetrafluoropropene (R1234ze (E)) as absorption working fluids. Int J Refrig 2018;88:45−57.

[35] Martín Á, Bermejo MD. Thermodynamic analysis of absorption refrigeration cycles using ionic liquid+ supercritical CO2 pairs. J Supercrit Fluids 2010;55(2):852−9.

[36] Smith JM, Van Ness HC, Abbott MM. Introduction to chemical engineering thermodynamics. sixth ed. New York: McGraw-Hill; 2002.

[37] Wu W, Wang B, You T, Wang J, Shi W, Li X. Compression-assisted absorption cycles using ammonia and various ionic liquids for cleaner heating. J Clean Prod 2018;195:890−907.

[38] NIST standard reference database 23. NIST reference fluid thermodynamic and transport properties−REFPROP, v9.1; 2013.

[39] Dong L, Zheng D, Nie N, Li Y. Performance prediction of absorption refrigeration cycle based on the measurements of vapor pressure and heat capacity of H2O+[DMIM] DMP system. Appl Energy 2012;98:326−32.

[40] Römich C, Merkel NC, Valbonesi A, Schaber K, Sauer S, Schubert TJ. Thermodynamic properties of binary mixtures of water and room-temperature ionic liquids: vapor pressures, heat capacities, densities, and viscosities of water+1-ethyl-3-methylimidazolium acetate and water+diethylmethylammonium methane sulfonate. J Chem Eng Data 2012;57(8):2258−64.

[41] Zhao J, Jiang XC, Li CX, Wang & ZH. Vapor pressure measurement for binary and ternary systems containing a phosphoric ionic liquid. Fluid Phase Equilib 2006;247:190−8.

[42] Zuo G, Zhao Z, Yan S, Zhang X. Thermodynamic properties of a new working pair: 1-Ethyl-3-methylimidazolium ethylsulfate and water. Chem Eng J 2010;156(3):613−7.

[43] Wang M, Becker TM, Ferreira CAI. Assessment of vapor−liquid equilibrium models for ionic liquid based working pairs in absorption cycles. Int J Refrig 2018;87:10−25.

[44] Boman DB, Hoysall DC, Staedter MA, Goyal A, Ponkala MJ, Garimella S. A method for comparison of absorption heat pump working pairs. Int J Refrig 2017;77:149−75.